Source location and valley shape effects on the *P–SV* near displacement field using a boundary integral equation–discrete wavenumber representation method

Stéphane Gaffet[1] and Michel Bouchon[2]

[1]*Laboratoire de Détection et de Géophysique, BP 12, 91680 Bruyères-le-Châtel, France*
[2]*IRIGM, Université Joseph Fourier, BP 53X, 38041 Grenoble Cedex, France*

SUMMARY

We use a numerical simulation to investigate the response of sediment-filled valleys to *P–SV* seismic excitation. The calculation is carried out using the discrete wavenumber–boundary integral equation method. We study in particular the case of explosion sources located within a basin or in its vicinity. We show that large amplification or defocusing effects are related to the source location and to the shape of the basin. In the case of complex basins made up of several sedimentary layers, waves propagating along the various interfaces play an important role in shaping the seismic response of the basin.

Key words: boundary integral method, defocusing, diffraction, explosion, heterogeneous media, wavenumber.

1 INTRODUCTION

The underground geological structure has a great influence on the observed seismic waveforms and can greatly affect the displacement amplitude as illustrated for instance by the work of Tucker & King (1984), or by the ground motion observed around Mexico City during the great 1985 Michoacán earthquake. In parallel with these observations, theoretical investigations have shown the important effects of the geometry of sedimentary basins and valleys on seismic motion (Aki & Larner 1970; Sánchez-Sesma & Esquivel 1979; Bard & Bouchon 1980a, 1980b, 1985; Bard & Gariel 1986; Campillo 1987; Sánchez-Sesma, Chávez-García & Bravo 1988; Kawase & Aki 1989). The aim of the present study is to extend these theoretical investigations to the case where the seismic excitation is a *P–SV* source, such as an explosion, and where the geological structure includes several irregular layers. We use the discrete wavenumber–boundary integral equation method previously described in an *SH* formulation (Bouchon, Campillo & Gaffet 1989). Following the study made on the topographic effects at short distances (Gaffet & Bouchon 1989) we investigate the effects of the source location and of the basin interface shape on the displacement field recorded by surface receivers at short distances from the source. The modifications induced on the diffracted field by the strong attenuation included in real structures are not studied. The investigations are only made for perfectly elastic media to give a good description of both the phase amplifications and the phase generations directly related to the heterogeneities.

2 DESCRIPTION OF THE METHOD

The method is described in the case of a semi-infinite space underlying a valley made up of a stack of laterally varying layers and bounded by a flat free surface (Fig. 1). The displacement field is computed frequency by frequency from the displacement potentials given by Lamb (1904) for horizontal and vertical forces acting at a point (x_p, z_p) of an infinite homogeneous elastic space. These compressional and shear potentials are written in a half-space formulation to directly cancel the tractions at the free surface. Following the approach developed by Bouchon & Aki (1977), we introduce a horizontal spatial periodicity X_L of the application point of force. This spatial periodicity induces a wavenumber space sampling with a step $\Delta k = 2\pi/X_L$. Two distributions of couples of horizontal and vertical forces located on the upper {i.e. $[Q_{P_l}^{h^{upper}} \exp{(i\omega t)}; Q_{P_l}^{v^{upper}} \exp{(i\omega t)}]$} and lower {i.e. $[Q_{P_l}^{h^{lower}} \exp{(i\omega t)}; Q_{P_l}^{v^{lower}} \exp{(i\omega t)}]$} sides of each interface l are used to represent the upward and downward elastic diffracted fields. These couples are regularly spaced at Δx sampling interval along the interfaces l ($l = 1, \ldots, L$). This sampling leads to a periodic wavenumber space restricting the wavenumber range to $[-\pi/\Delta x; +\pi/\Delta x]$. The representation of the
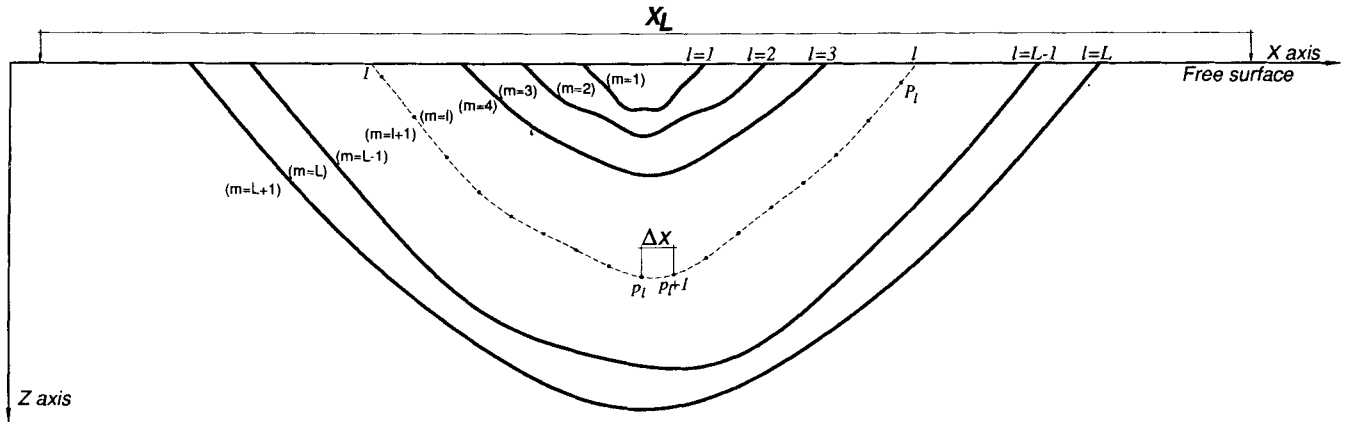
Figure 1. Medium geometry and description of the different notations. The medium is described by $l = 1, \ldots, L$ interfaces defining $m = 1, \ldots, L + 1$ layers. The interface sampling step is Δx along the x axis. The periodicity of the medium is X_L (see text for explanations).

diffracted field can be made as precise as desired when reducing Δx. The amplitudes Q_{Pl}^{hupper}, Q_{Pl}^{vupper}, Q_{Pl}^{hlower}, and Q_{Pl}^{vlower} are determined to ensure the continuity of the displacement-traction field across the interfaces.

Using the formulation given by Gaffet & Bouchon (1989), the compressional and shear displacement potentials for a distribution of P_l horizontal forces regularly spaced along an interface l in a periodic elastic homogeneous half-space are given by

$$\phi_{h,l}^{1/2 \text{ space}} = F \sum_{p_l=1}^{p_l=P_l} Q_{Pl}^{h} \sum_{n=-M}^{n=+M} \left(\frac{k_n}{v_n} E_{npl} + \frac{k_n}{v_n} R_{PP} T_{npl} + R_{SP} V_{npl} \right) H_{npl}, \tag{1}$$

$$\psi_{h,l}^{1/2 \text{ space}} = F \sum_{p_l=1}^{p_l=P_l} Q_{Pl}^{h} \sum_{n=-M}^{n=+M} \left(-\text{sign} \, (z - z_{pl}) G_{npl} + R_{SS} U_{npl} + \frac{k_n}{v_n} R_{PS} W_{npl} \right) H_{npl}. \tag{2}$$

Similarly we obtain for a distribution of P_l vertical forces

$$\phi_{v,l}^{1/2 \text{ space}} = F \sum_{p_l=1}^{p_l=P_l} Q_{Pl}^{v} \sum_{n=-M}^{n=+M} \left(\text{sign} \, (z - z_{pl}) E_{npl} - R_{PP} T_{npl} + \frac{k_n}{\gamma_n} R_{SP} V_{npl} \right) H_{npl}, \tag{3}$$

$$\psi_{v,l}^{1/2 \text{ space}} = F \sum_{p_l=1}^{p_l=P_l} Q_{Pl}^{v} \sum_{n=-M}^{n=+M} \left(\frac{k_n}{\gamma_n} G_{npl} + \frac{k_n}{\gamma_n} R_{SS} U_{npl} - R_{PS} W_{npl} \right) H_{npl}. \tag{4}$$

with

$$F = 1/2 X_L \omega^2 \rho, \qquad E_{npl} = \exp\,(-iv_n \,|z - z_{pl}|), \qquad G_{npl} = \exp\,(-i\gamma_n \,|z - z_{pl}|),$$

$$H_{npl} = \exp\,[-ik_n(x - x_{pl})], \qquad T_{npl} = \exp[-iv_n(z - z_{pl})], \qquad U_{npl} = \exp\,[-i\gamma_n(z - z_{pl})], \tag{5}$$

$$V_{npl} = \exp\,(-iv_n z - i\gamma_n z_{pl}), \qquad W_{npl} = \exp\,(-i\gamma_n z - v_n z_{pl}),$$

where $M = \pi/(\Delta k \, \Delta x)$, $k_n = 2n\pi/X_L$, $v_n^2 = \omega^2/\alpha^2 - k_n^2$, $\gamma_n^2 = \omega^2/\beta^2 - k_n^2$, $\mathscr{I}m(v_n) \leq 0$ and $\mathscr{I}m(\gamma_n) \leq 0$. ω denotes the angular frequency, α and β are the compressional and the shear wave velocities, and ρ is the density. R_{PP}, R_{PS}, R_{SP}, and R_{SS} are the reflection coefficients of the potentials at the free surface and are dependent upon k_n, v_n, and γ_n. The horizontal and vertical displacements in a 2-D Cartesian space are obtained using Helmholtz' formulae:

$$u(x, z) = \frac{\partial(\phi_h + \phi_v)}{\partial x} - \frac{\partial(\psi_h + \psi_v)}{\partial z}, \qquad w(x, z) = \frac{\partial(\phi_h + \phi_v)}{\partial z} + \frac{\partial(\psi_h + \psi_v)}{\partial x}. \tag{6}$$

The stress tensor components are obtained using Hooke's law. Defining the terms

$$a_n^{xx} = (\lambda + 2\mu)k_n^2 + \lambda v_n^2, \qquad a_n^{xz} = 2\mu k_n v_n, \qquad b_n^{xx} = 2\mu k_n \gamma_n, \qquad b_n^{xz} = \mu(k_n^2 - \gamma_n^2),$$

$$C_{npl} = 2 \cos\,[k_n(x - x_{pl})], \qquad S_{npl} = -2i \sin\,[k_n(x - x_{pl})], \tag{7}$$

we obtain the displacements and tractions for each point (x, z) of the space for (i) a distribution of P_l horizontal forces regularly spaced along an interface l:

$$u^h(x, z) = -iF \sum_{p_l=1}^{p_l=P_l} Q_{Pl}^{h} \left[-\gamma_0 \xi_{0pl}^{h} + \sum_{n=1}^{n=M} C_{npl}(k_n \kappa_{npl}^{h} - \gamma_n \xi_{npl}^{h}) \right], \tag{8}$$

$$w^h(x, z) = -iF \sum_{p_l=1}^{p_l=P_l} Q_{p_l}^h \left[\sum_{n=1}^{n=M} S_{np_l} (v_n \zeta_{np_l}^h + k_n \kappa_{np_l}^h) \right], \tag{9}$$

$$\sigma_{xx}^h(x, z) = -F \sum_{p_l=1}^{p_l=P_l} Q_{p_l}^h \left[\sum_{n=1}^{n=M} S_{np_l} (a_n^{xx} \kappa_{np_l}^h - b_n^{xx} \xi_{np_l}^h) \right], \tag{10}$$

$$\sigma_{xz}^h(x, z) = -F \sum_{p_l=1}^{p_l=P_l} Q_{p_l}^h \left[b_0^{xz} \chi_{0p_l}^h + \sum_{n=1}^{n=M} C_{np_l} (a_n^{xz} \zeta_{np_l}^h + b_n^{xz} \chi_{np_l}^h) \right], \tag{11}$$

$$\sigma_{zz}^h(x, z) = -F \sum_{p_l=1}^{p_l=P_l} Q_{p_l}^h \left[\sum_{n=1}^{n=M} S_{np_l} (-b_n^{xz} \kappa_{np_l}^h + b_n^{xx} \xi_{np_l}^h) \right], \tag{12}$$

where

$$\kappa_{np_l}^h = \frac{k_n}{v_n} E_{np_l} + \frac{k_n}{v_n} R_{PP} T_{np_l} + R_{SP} V_{np_l}, \qquad \chi_{np_l}^h = -\text{sign} (z - z_{p_l}) G_{np_l} + R_{SS} U_{np_l} + \frac{k_n}{v_n} R_{PS} W_{np_l},$$

$$\zeta_{np_l}^h = \text{sign} (z - z_{p_l}) \frac{k_n}{v_n} E_{np_l} + \frac{k_n}{v_n} R_{PP} T_{np_l} + R_{SP} V_{np_l}, \qquad \xi_{np_l}^h = -G_{np_l} + R_{SS} U_{np_l} + \frac{k_n}{v_n} R_{PS} W_{np_l}, \tag{13}$$

and (ii) for a distribution of P_l vertical forces

$$u^v(x, z) = -iF \sum_{p_l=1}^{p_l=P_l} Q_{p_l}^v \left[\sum_{n=1}^{n=M} S_{np_l} (k_n \kappa_{np_l}^v - \gamma_n \xi_{np_l}^v) \right], \tag{14}$$

$$w^v(x, z) = -iF \sum_{p_l=1}^{p_l=P_l} Q_{p_l}^v \left[v_0 \zeta_{0p_l} + \sum_{n=1}^{n=M} C_{np_l} (v_n \zeta_{np_l}^v + k_n \kappa_{np_l}^v) \right], \tag{15}$$

$$\sigma_{xx}^v(x, z) = -F \sum_{p_l=1}^{p_l=P_l} Q_{p_l}^v \left[a_0^{xx} \kappa_{0p_l} + \sum_{n=1}^{n=M} C_{np_l} (a_n^{xx} \kappa_{np_l}^v - b_n^{xx} \xi_{np_l}^v) \right], \tag{16}$$

$$\sigma_{xz}^v(x, z) = -F \sum_{p_l=1}^{p_l=P_l} Q_{p_l}^v \left[\sum_{n=1}^{n=M} S_{np_l} (a_n^{xz} \zeta_{np_l}^v + b_n^{xz} \chi_{np_l}^v) \right], \tag{17}$$

$$\sigma_{zz}^v(x, z) = -F \sum_{p_l=1}^{p_l=P_l} Q_{p_l}^v \left[-b_0^{xz} \kappa_{0p_l} + \sum_{n=1}^{n=M} C_{np_l} (-b_n^{xz} \kappa_{np_l}^v + b_n^{xx} \xi_{np_l}^v) \right], \tag{18}$$

where

$$\kappa_{np_l}^v = \text{sign} (z - z_{p_l}) E_{np_l} - R_{PP} T_{np_l} + \frac{k_n}{\gamma_n} R_{SP} V_{np_l}, \qquad \chi_{np_l}^v = \frac{k_n}{\gamma_n} G_{np_l} + \frac{k_n}{\gamma_n} R_{SS} U_{np_l} - R_{PS} W_{np_l},$$

$$\zeta_{np_l}^v = E_{np_l} - R_{PP} T_{np_l} + \frac{k_n}{\gamma_n} R_{SP} V_{np_l}, \qquad \xi_{np_l}^v = \text{sign} (z - z_{p_l}) \frac{k_n}{\gamma_n} G_{np_l} + \frac{k_n}{\gamma_n} R_{SS} U_{np_l} - R_{PS} W_{np_l}. \tag{19}$$

The forces applied on the upper and lower sides of an interface must ensure the continuity of the displacement-traction field across this interface. We define a displacement-traction vector $\mathbf{S}_{s,l}^{(m)} = [\mathbf{U}_{s,l}^{(m)}; \mathbf{T}_{s,l}^{(m)}(\mathbf{n}_l^{(m)})]^T$, where

$$\mathbf{U}_{s,l}^{(m)} = [u_x^{(m)}(x_{1_l}, z_{1_l}), \ldots, u_x^{(m)}(x_{P_l}, z_{P_l}), u_z^{(m)}(x_{1_l}, z_{1_l}), \ldots, u_z^{(m)}(x_{P_l}, z_{P_l})]$$

is the displacement vector and where $u_x^{(m)}(x_{p_l}, z_{p_l})$ and $u_z^{(m)}(x_{p_l}, z_{p_l})$ are the horizontal and vertical components of the displacement in medium m at each sampling point (x_{p_l}, z_{p_l}) of the interface l and produced by a source s located in medium m.

$$\mathbf{T}_{s,l}^{(m)} = [T_x^{(m)}(x_{1_l}, z_{1_l}), \ldots, T_x^{(m)}(x_{P_l}, z_{P_l}), T_z^{(m)}(x_{1_l}, z_{1_l}), \ldots, T_z^{(m)}(x_{P_l}, z_{P_l})]$$

is the traction vector for which each component is defined as the product of the stress tensor σ induced by a source s acting in medium m by the unit vector $\mathbf{n}_l^{(m)}$ normal to the interface l and pointing outward relatively to medium m at the point (x_{p_l}, z_{p_l}), i.e.

$$T_x^{(m)}(x_{p_l}, z_{p_l}) = \sigma_{xx}^s(x_{p_l}, z_{p_l}) n_{x,l}^{(m)}(x_{p_l}, z_{p_l}) + \sigma_{xz}^s(x_{p_l}, z_{p_l}) n_{z,l}^{(m)}(x_{p_l}, z_{p_l}),$$

$$T_z^{(m)}(x_{p_l}, z_{p_l}) = \sigma_{xz}^s(x_{p_l}, z_{p_l}) n_{x,l}^{(m)}(x_{p_l}, z_{p_l}) + \sigma_{zz}^s(x_{p_l}, z_{p_l}) n_{z,l}^{(m)}(x_{p_l}, z_{p_l}). \tag{20}$$

Assuming the existence of one or more source(s) in each medium, we have to solve the following linear matrix system:

$$
\begin{aligned}
\mathbf{S}_{1,1}^{(1)} + \mathbf{A}_{1,1}^{(1)}\mathbf{Q}_1^{\text{upper}} &= \mathbf{S}_{2,1}^{(2)} + \mathbf{A}_{1,1}^{(2)}\mathbf{Q}_1^{\text{lower}} + \mathbf{A}_{2,1}^{(2)}\mathbf{Q}_2^{\text{upper}}, \\
\mathbf{S}_{2,2}^{(2)} + \mathbf{A}_{2,2}^{(2)}\mathbf{Q}_2^{\text{upper}} + \mathbf{A}_{1,2}^{(2)}\mathbf{Q}_1^{\text{lower}} &= \mathbf{S}_{3,2}^{(2)} + \mathbf{A}_{2,2}^{(3)}\mathbf{Q}_2^{\text{lower}} + \mathbf{A}_{3,2}^{(3)}\mathbf{Q}_3^{\text{upper}}, \\
&\vdots \\
\mathbf{S}_{l,l}^{(l)} + \mathbf{A}_{l,l}^{(l)}\mathbf{Q}_l^{\text{upper}} + \mathbf{A}_{l-1,l}^{(l)}\mathbf{Q}_{l-1}^{\text{lower}} &= \mathbf{S}_{l+1,l}^{(l+1)} + \mathbf{A}_{l,l}^{(l+1)}\mathbf{Q}_l^{\text{lower}} + \mathbf{A}_{l+1,l}^{(l+1)}\mathbf{Q}_{l+1}^{\text{upper}}, \\
&\vdots \\
\mathbf{S}_{L,L}^{(L)} + \mathbf{A}_{L,L}^{(L)}\mathbf{Q}_L^{\text{upper}} + \mathbf{A}_{L-1,L}^{(L)}\mathbf{Q}_{L-1}^{\text{lower}} &= \mathbf{S}_{L+1,L}^{(L+1)} + \mathbf{A}_{L,L}^{(L+1)}\mathbf{Q}_L^{\text{lower}},
\end{aligned}
\tag{21}
$$

where $\mathbf{S}_{m,l}^{(m)}$ is the displacement-traction vector acting on the sampling points of the interface l in medium m and due to the source located in medium m. $\mathbf{A}_{l1,l2}^{(m)}\mathbf{Q}_{l1}^{\text{upper}}$ is the displacement-traction vector acting on the sampling points of the interface $l2$ in medium m and due to the force distribution $\mathbf{Q}^{\text{upper}}$ applied on the upper side of interface $l1$. $\mathbf{A}_{l1,l2}^{(m)}\mathbf{Q}_{l1}^{\text{lower}}$ is the displacement-traction vector acting on the sampling points of interface $l2$ in the medium m and due to the force distribution $\mathbf{Q}^{\text{lower}}$ applied on the lower side of interface $l1$.

The coefficients of the matrix $\mathbf{A}_{l1,l2}^{(m)}$ are deduced from equations (8) to (12), and (14) to (19). To solve this system leads us to determine the vectors $\mathbf{Q}_l = (\mathbf{Q}_l^{\text{upper}}; \mathbf{Q}_l^{\text{lower}})$ which contain the unknown forces applied on the upper or lower sides of the interfaces $l = 1, \ldots, L$. The general solution is given by the following recurrent algorithm:

$$
\begin{aligned}
\mathbf{Q}_1 &= \mathbf{a}_1(-\mathbf{S}_{1,1}^{(1)} + \mathbf{S}_{2,1}^{(2)}) + \mathbf{b}_1\mathbf{Q}_2^{\text{upper}} \quad \text{with} &
\mathbf{a}_1 &= (\mathbf{A}_{1,1}^{(1)}; -\mathbf{A}_{1,1}^{(1)})^{-1} \quad \text{and} &
\mathbf{b}_1 &= \mathbf{a}_1\mathbf{A}_{2,1}^{(2)}, \\
\mathbf{Q}_2 &= \mathbf{a}_2(-\mathbf{S}_{2,2}^{(2)} + \mathbf{S}_{3,2}^{(3)} - \mathbf{A}_{1,2}^{(2)}\mathbf{Q}_1^{\text{lower}}) + \mathbf{b}_2\mathbf{Q}_3^{\text{upper}}, &
\mathbf{a}_2 &= (\mathbf{A}_{1,2}^{(2)}\mathbf{b}_1^{\text{lower}} + \mathbf{A}_{2,2}^{(2)}; -\mathbf{A}_{2,2}^{(3)})^{-1} \quad \text{and} &
\mathbf{b}_2 &= \mathbf{a}_2\mathbf{A}_{3,2}^{(3)}, \\
&\vdots \\
\mathbf{Q}_l &= \mathbf{a}_l(-\mathbf{S}_{l,l}^{(l)} + \mathbf{S}_{l+1,l}^{(l+1)} - \mathbf{A}_{l-1,l}^{(l)}\mathbf{Q}_{l-1}^{\text{lower}}) + \mathbf{b}_l\mathbf{Q}_{l+1}^{\text{upper}}, &
\mathbf{a}_l &= (\mathbf{A}_{l-1,l}^{l}\mathbf{b}_{l-1}^{\text{lower}} + \mathbf{A}_{l,l}^{(l)}; -\mathbf{A}_{l,l}^{(l+1)})^{-1} \quad \text{and} \quad \mathbf{b}_l = \mathbf{a}_l\mathbf{A}_{l+1,l}^{(l+1)}, \\
&\vdots \\
\mathbf{Q}_L &= \mathbf{a}_L(-\mathbf{S}_{L,L}^{(L)} + \mathbf{S}_{L+1,L}^{(L+1)} - \mathbf{A}_{L-1,L}^{(L)}\mathbf{Q}_{L-1}^{\text{lower}}), &
\mathbf{a}_L &= (\mathbf{A}_{L-1,L}^{(L)}\mathbf{b}_{L-1}^{\text{lower}} + \mathbf{A}_{L,L}^{(L)}; -\mathbf{A}_{L,L}^{(L+1)})^{-1},
\end{aligned}
\tag{22}
$$

where $\mathbf{b}_l$ is a $4P_l \times 2P_{l+1}$ matrix and $\mathbf{b}_l^{\text{lower}}$ represents the $2P_{l+1} \times 2P_{l+1}$ square matrix extracted from the lower part of $\mathbf{b}_l$. P_l is the number of sampling points of the interface l (Fig. 1). The algorithm has been here described in the tutorial case of non-intersecting layers. The method is however not restricted to this case and can be developed for more general configurations (e.g. for intersecting or non-intersecting layers as well as for cross bed or horizontal irregular stratum).

The use of (21) requires to formulate the terms $\mathbf{S}_{m,l}^{(m)}$ for different kinds of source (e.g. explosion or double couple sources). We give here the expressions of the compressional and of the shear displacement potentials for an explosion which occurred at a point (x_m, z_m) of the half-space. The explosive source is made up of two force dipoles orthogonal to each other. That is to say the potentials of this source derive from the potentials given by Lamb (1904) for horizontal and vertical forces. Thus

$$
\phi_{\text{explosion}}^{1/2\,\text{space}} = \frac{\partial \phi_{\text{h}}^{1/2\,\text{space}}}{\partial x_m} + \frac{\partial \phi_{\text{v}}^{1/2\,\text{space}}}{\partial z_m}, \qquad
\psi_{\text{explosion}}^{1/2\,\text{space}} = \frac{\partial \psi_{\text{h}}^{1/2\,\text{space}}}{\partial x_m} + \frac{\partial \psi_{\text{v}}^{1/2\,\text{space}}}{\partial z_m},
\tag{23}
$$

with

$$
\phi_{\text{explosion}}^{1/2\,\text{space}} = ik_\alpha^2 F \sum_{n=-N_{\text{conv}}}^{+N_{\text{conv}}} \frac{1}{v_n}(E_{nm} + R_{PP}T_{nm})H_{nm}, \qquad
\psi_{\text{explosion}}^{1/2\,\text{space}} = ik_\alpha^2 F \sum_{n=-N_{\text{conv}}}^{+N_{\text{conv}}} \frac{1}{v_n} R_{PS}W_{nm}H_{nm},
\tag{24}
$$

where $k_\alpha = \omega/\alpha$ and where N_{conv} is the summation limit that ensures the convergence of the series at the observation point (x, z). Similarly the displacement potentials for a double couple source in the reference axes given in Fig. 1 are

$$
\begin{aligned}
\phi_{\text{double couple}}^{1/2\,\text{space}} &= d_1\left(\frac{\partial \phi_{\text{h}}^{1/2\,\text{space}}}{\partial x_m} - \frac{\partial \phi_{\text{v}}^{1/2\,\text{space}}}{\partial z_m}\right) + d_2\left(\frac{\partial \phi_{\text{h}}^{1/2\,\text{space}}}{\partial z_m} + \frac{\partial \phi_{\text{v}}^{1/2\,\text{space}}}{\partial x_m}\right), \\
\psi_{\text{double couple}}^{1/2\,\text{space}} &= d_1\left(\frac{\partial \psi_{\text{h}}^{1/2\,\text{space}}}{\partial x_m} - \frac{\partial \psi_{\text{v}}^{1/2\,\text{space}}}{\partial z_m}\right) + d_2\left(\frac{\partial \psi_{\text{h}}^{1/2\,\text{space}}}{\partial z_m} + \frac{\partial \psi_{\text{v}}^{1/2\,\text{space}}}{\partial x_m}\right),
\end{aligned}
\tag{25}
$$

with $d_1 = -\sin(2\theta)$ and $d_2 = -\cos(2\theta)$ and where θ is the counterclockwise angle between the horizontal axis and the double

couple orientation; we then obtain

$$\phi_{\text{double couple}}^{1/2 \text{ space}} = iF \sum_{n=-N_{\text{conv}}}^{+N_{\text{conv}}} \left\{ \left[d_1\left(\frac{k_n^2}{v_n} - v_n\right) + 2d_2 k_n \text{ sign } (z - z_m) \right] E_{nm} + \left[d_1\left(\frac{k_n^2}{v_n} - v_n\right) - 2d_2 k_n \right] R_{PP} T_{nm} \right.$$

$$\left. + \left[2d_1 k_n + d_2\left(\frac{k_n^2}{\gamma_n} - \gamma_n\right) \right] R_{SP}^{'} V_{nm} \right\} H_{nm},$$

$$\psi_{\text{double couple}}^{1/2 \text{ space}} = iF \sum_{n=-N_{\text{conv}}}^{+N_{\text{conv}}} \left\{ \left[d_2\left(\frac{k_n^2}{\gamma_n} - \gamma_n\right) - 2d_1 k_n \text{ sign } (z - z_m) \right] G_{nm} + \left[d_2\left(\frac{k_n^2}{\gamma_n} - \gamma_n\right) + 2d_1 k_n \right] R_{SS} U_{nm} \right.$$

$$\left. + \left[-2d_2 k_n + d_1\left(\frac{k_n^2}{v_n} - v_n\right) \right] R_{PS} W_{nm} \right\} H_{nm}.$$

(26)

3 APPLICATIONS

3.1 Tests of the method

The displacement fields computed in the case of plane *P*- and *SV*-waves vertically incident upon the valley depicted in Fig. 2 are displayed in a contour map form Figs 3 and 4. In order to check the method we use it in the medium configuration given
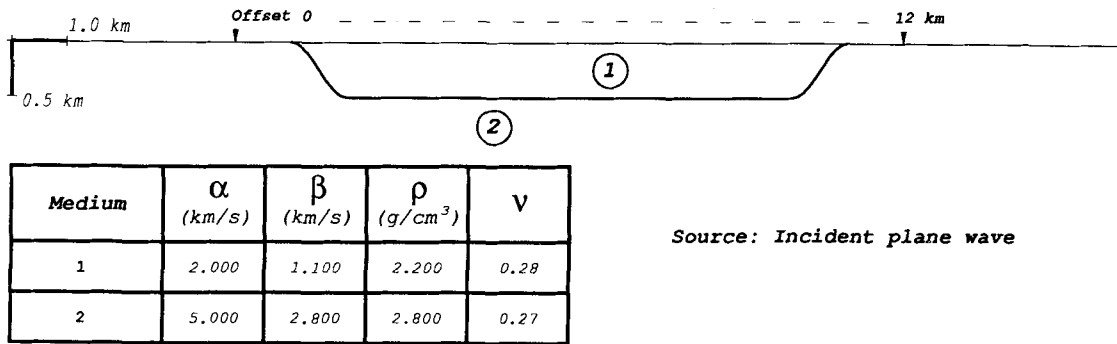

Medium	α (km/s)	β (km/s)	ρ (g/cm^3)	ν
1	2.000	1.100	2.200	0.28
2	5.000	2.800	2.800	0.27

Source: Incident plane wave

Figure 2. Medium geometry for the first computation and location of the receiver array from offset 0 to offset 12 km. The medium is made up of a thin and flat sedimentary valley whose elastic parameters are summarized in the table. Medium 1 corresponds to the valley, and medium 2 to the underlying bedrock. The sources considered are vertically incident plane *P*- and *SV*-waves. α, β, ρ, and ν correspond respectively to the *P*- and *S*-wave velocities, to the density and to the Poisson's ratio of each medium.

— — *Normal incident plane* P—wave — — *Type II valley* — —

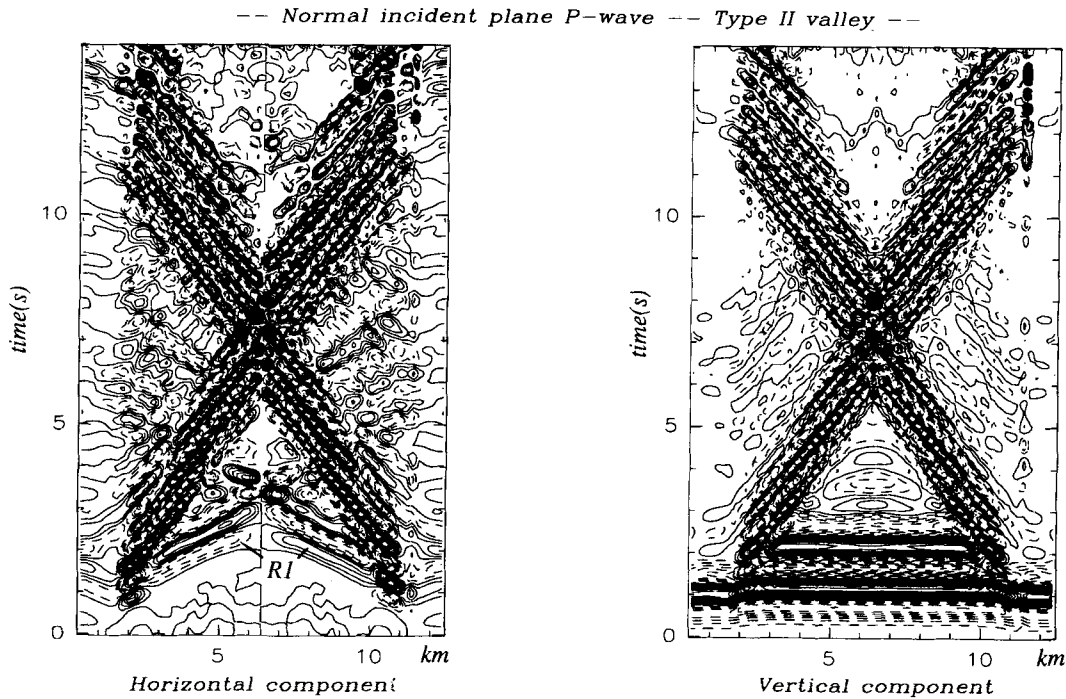*Horizontal component*   *Vertical component*

Figure 3. Contour map representations for the horizontal (left-hand) and the vertical (right-hand) components of the displacement field recorded by the surface receivers depicted in Fig. 2. The source is a vertically incident plane *P*-wave having a Ricker time dependence in displacement with a characteristic period of 1.16 s.

Normal incident plane SV—wave — — Type II valley — —

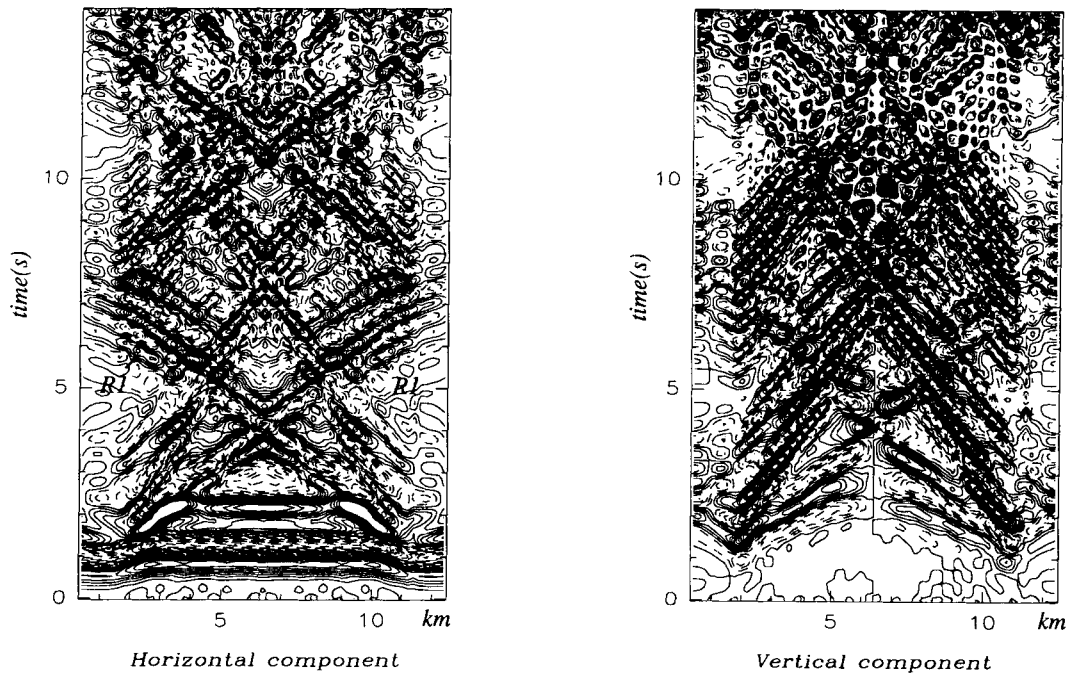Horizontal component   Vertical component

Figure 4. Same as Fig. 3 for a vertically incident plane *SV*-wave.

Fig. 2 that corresponds to the low velocity contrast valley type II considered by Bard & Bouchon (1980b). In both Figs 3 and 4 the left- and the right-hand sides show respectively the horizontal and the vertical components of the ground motion. The time window associated with the vertical axis is 15 s long and the station offsets are presented on the horizontal axis in kilometre units. The source time function is a Ricker wavelet having a characteristic period of 1.16 s. (i) In the case of the vertically incident plane *P*-wave (Fig. 3) we observe besides the direct arrival two surface wavetrains with a 1.2 Hz almost stationary frequency. The maximum amplitude of these waves travels across the basin with a phase velocity of 1.15 km s^{-1}. These waves have been generated at each edge of the valley and correspond to the fundamental mode of the Rayleigh wave (see the phase
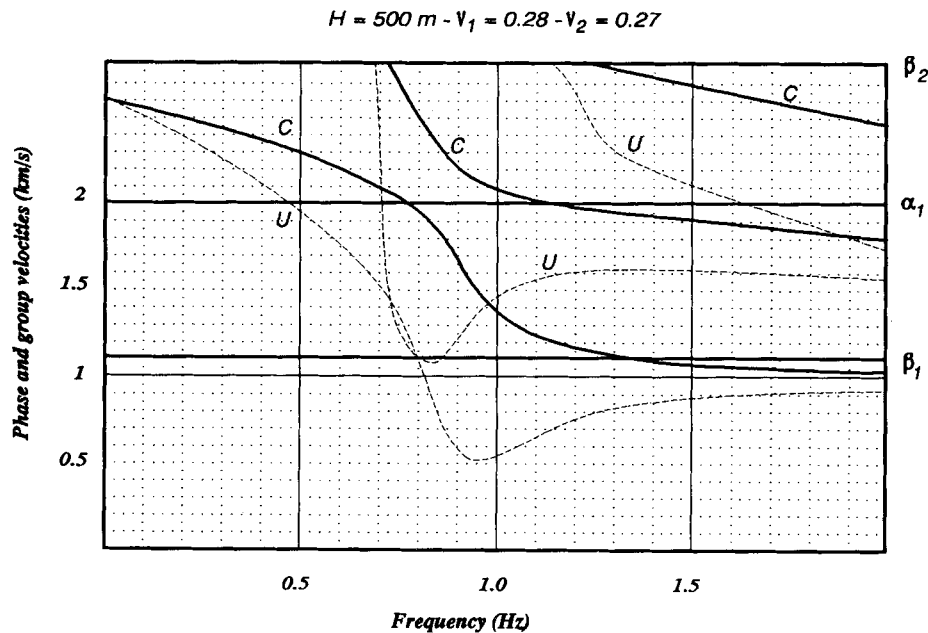
H = 500 m - V_1 = 0.28 - V_2 = 0.27

Figure 5. Phase and group velocities (the thick bold lines, c, and the thin broken ones, u respectively) versus frequency diagram computed for a medium equivalent to the medium given in Fig. 2 and made up of a layer having a thickness of 0.5 km overlying a half-space. The elastic characteristics of the layer and of the half-space are the same as those described in Fig. 2.
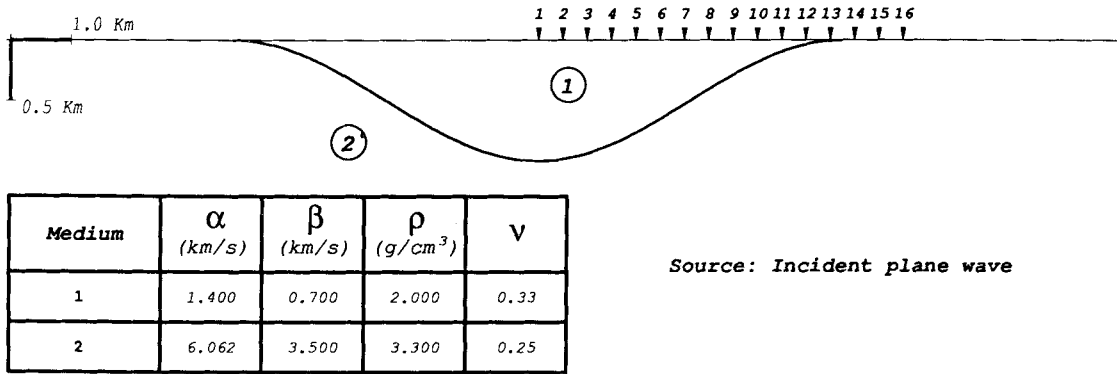
Medium	α (km/s)	β (km/s)	ρ (g/cm³)	ν
1	1.400	0.700	2.000	0.33
2	6.062	3.500	3.300	0.25

Source: Incident plane wave

Figure 6. Medium geometry and location of the 16 receivers. The medium is made up of a sediment-filled valley whose elastic parameters are summarized in the table. The notations are the same as in Fig. 2.

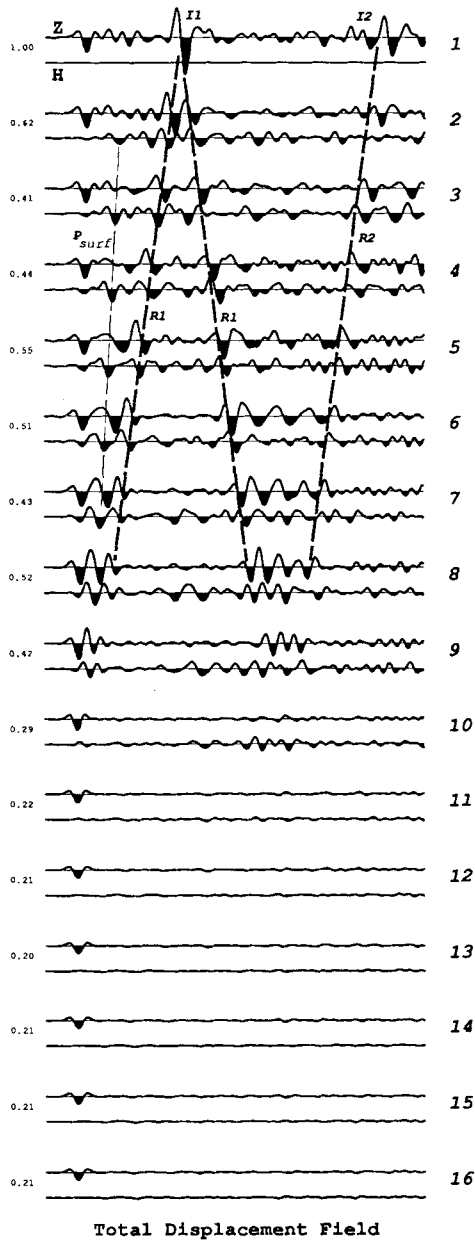*Time window: 23.50 sec. - Source frequency: 0.70 Hz*

Total Displacement Field

Figure 7. Representation of the horizontal **H** and vertical **Z** displacement components recorded at the 16 receivers displayed in Fig. 6. The time duration is 23.5 s long and the Ricker frequency equals 0.7 Hz. See explanation in the text concerning the notation I1, I2, R1, and R2.

and group velocities versus frequency diagram given Fig. 5). This mode prevails in the diffracted field but the first higher mode of the Rayleigh wave slightly appears in the earlier part of the horizontal component. This phase has been emphasized by the R1 mark drawn on the horizontal map (Fig. 3). (ii) The diffracted field obtained in the case of the vertically incident plane SV-wave (Fig. 4) is more complex. This can be explained by the greater excitation of the first higher mode of the Rayleigh wave for an incident SV-plane wave. This mode propagates with a 1.9 km s^{-1} phase velocity at a 1.4 Hz frequency. This mode which is well observed on the horizontal displacement component (i.e. the phase marked R1), is reflected at the edges of the basin (i.e. see the mark R1). The amplitude of this horizontally polarized mode is now comparable to the amplitude of the fundamental mode that continues to prevail on the vertical component.

We now check the method with a configuration that illustrates the completeness of the computed diffracted displacement field. The medium corresponds to the high velocity contrast valley type I (Fig. 6) defined by Bard & Bouchon (1980b). The seismograms are computed over a time window of 23.5 s at 16 receivers with a Ricker source time dependence having a 0.7 Hz central frequency. The elastic parameters of the model are recalled in Fig. 6. The source is a vertically incident plane P-wave. The seismograms are presented in Fig. 7. Besides the direct P arrival one can see two different types of propagating waves emphasized by the thin broken line signed P_{surf} and by the thick bold broken lines denoted R1 and R2. The P_{surf} marked phase propagates with the basin P-wave velocity. It has a prevailing horizontal component and corresponds to the surface P-wave described by Lapwood (1949) and Bouchon (1978). This phase generated at the edge of the basin has an amplitude equal to two thirds of the amplitude of the phases R1. The phases R1 travelling across the basin with a 0.65 km s^{-1} phase velocity have a predominant vertical motion and correspond to two Rayleigh waves symetrically generated at the two edges of the basin. These two surface waves interfere at the centre of the basin resulting in a strong increase of the Rayleigh pulse at the receiver 1 (see the mark I1 Fig. 7). Each Rayleigh phase (i.e. R1) is reflected at each edge and backpropagates across the valley (see the mark R2 Fig. 7), generating a new interference at the receiver 1 (see the mark I2 Fig. 7).

3.2 Effect of source location within the basin

The medium considered here corresponds to the profile across the central region of Yucca Flat valley, Nevada, given by Ferguson (1988). The basin interface used is an idealized interpolation of the interface between the Tertiary volcanic rocks and the Palaeozoic basement. The basin is assumed to be filled only with Tertiary volcanic saturated materials. Neither the water table nor the alluvium layer are taken into account in the model in order to focus the attention on the influence of the source location within the basin on the displacement field at short distances. The medium geometry and the elastic parameters are those given by Ferguson (1988) and are depicted in Fig. 8. The four maximum slope angles observed from the left-hand side to the right-hand side of the basin interface are 21°, 9°, 6°, and 40°. Four explosions of same energy and buried at 600 m depth (i.e. A, B, C, and D) are used for this study. The computed seismograms are displayed in Figs 9(a), (b), (c) and (d). The time window is 15 s long and the source time function in displacement is a Ricker pulse having a 0.75 Hz central frequency. The seismogram displays have been normalized for each receiver. The absolute amplitude scales are given at the left of each receiver for all detonations to allow us to directly compare all the seismogram amplitudes. The receiver spacings are reproduced to clearly show the existing phases.

The large maximum amplitude variations observed between the different configurations [i.e. the factor 1.78 observed at receiver h Fig. 9(c)] is correlated to the vicinity of the basement straight below explosion C. For this explosion, the absolute amplitudes of the field diffracted inside and in the right side of the basin are greater than in the case of the three other
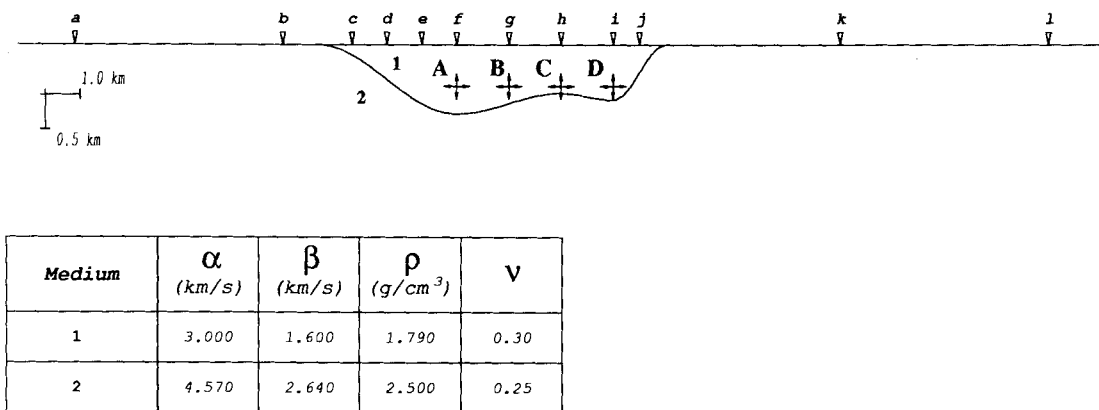
Medium	α (km/s)	β (km/s)	ρ (g/cm^3)	ν
1	3.000	1.600	1.790	0.30
2	4.570	2.640	2.500	0.25

Figure 8. Medium geometry and location of the 12 receivers and of the four detonations considered for the calculation.

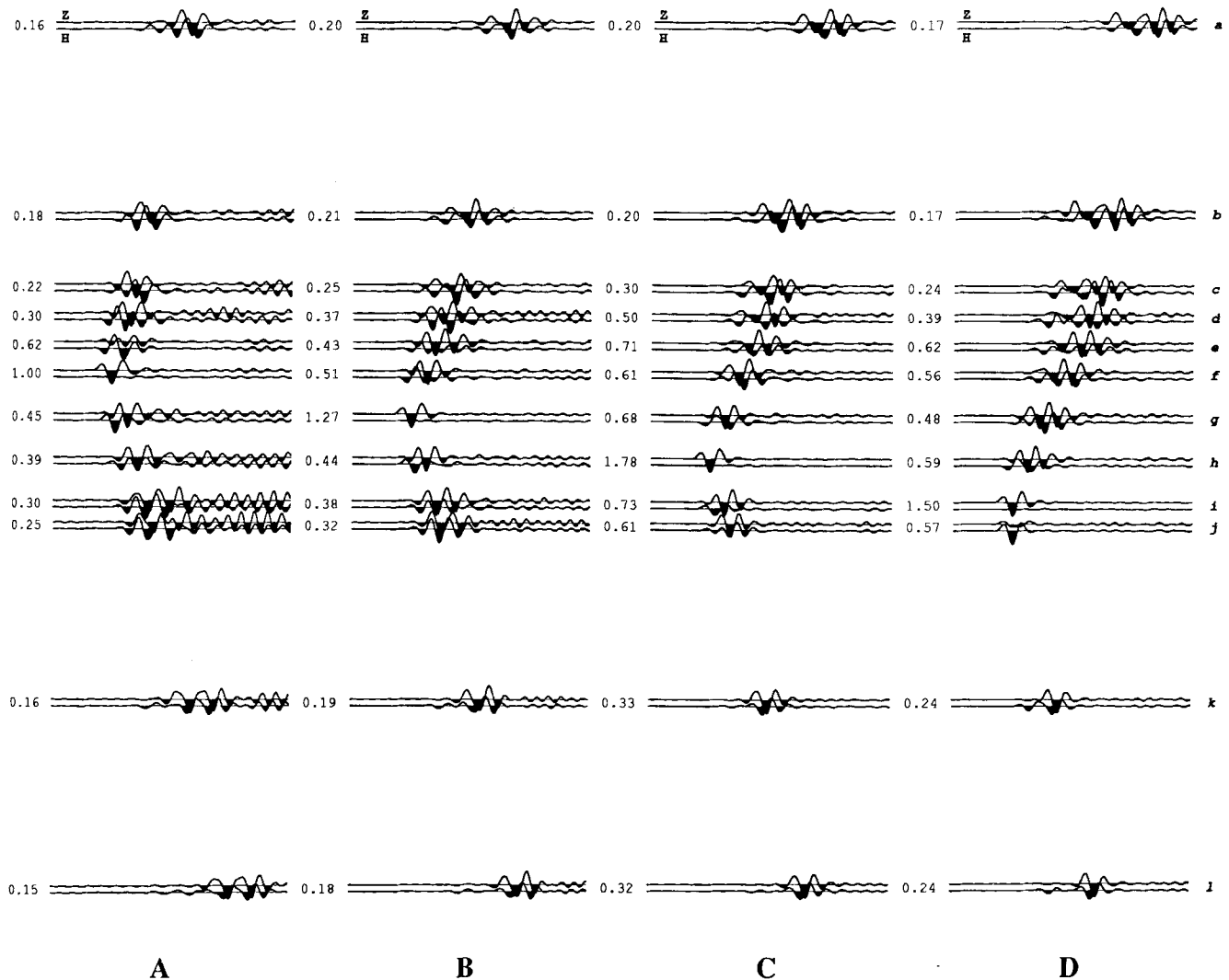0.16 $\frac{Z}{H}$ ———————⌒◇◇— 0.20 $\frac{Z}{H}$ ——————⌒∿◇— 0.20 $\frac{Z}{H}$ ————⌒∿◇— 0.17 $\frac{Z}{H}$ ————⌒∿◇◇— **a**

0.18 ————∿◇◇— 0.21 ————∿◇◇— 0.20 ————∿◇◇— 0.17 ————∿◇◇— **b**

0.22 ——∿◇◇◇— 0.25 ——∿◇◇— 0.30 ——∿◇◇— 0.24 ——∿◇◇— **c**

0.30 ——∿◇◇◇— 0.37 ——∿◇◇— 0.50 ——∿◇◇— 0.39 ——∿◇◇— **d**

0.62 ——∿◇◇— 0.43 ——∿◇◇— 0.71 ——∿◇◇— 0.62 ——∿◇◇— **e**

1.00 ——◇◇— 0.51 ——∿◇— 0.61 ——◇◇— 0.56 ——∿◇— **f**

0.45 ——∿◇◇— 1.27 ——◇◇— 0.68 ——◇◇— 0.48 ——◇◇— **g**

0.39 ——∿◇◇◇◇◇— 0.44 ——∿◇◇— 1.78 ——∿— 0.59 ——∿◇◇— **h**

0.30 ——∿◇◇◇◇◇— 0.38 ——∿◇◇◇— 0.73 ——∿◇◇— 1.50 ——∿◇— **i**

0.25 ——∿◇◇◇◇◇— 0.32 ——∿◇◇◇— 0.61 ——∿◇◇— 0.57 ——∿— **j**

0.16 ——∿◇◇◇◇— 0.19 ——∿◇◇◇— 0.33 ——∿◇◇— 0.24 ——∿◇◇— **k**

0.15 ——∿◇◇◇— 0.18 ——∿◇◇— 0.32 ——∿◇◇— 0.24 ——∿◇— **l**

A   **B**   **C**   **D**

Figure 9. Representation of the horizontal **H** and vertical **Z** components of the seismograms computed at the 12 surface receivers for the explosions A, B, C, and D detonated in the medium defined in Fig. 8. The time window lasts for 15 s, the central Ricker source frequency is 0.75 Hz. The relative amplitudes are used to draw the seismograms and the amplitudes written at the left of the traces are the absolute ones for the four explosions studies. (a), (b), (c), and (d) correspond respectively to the A, B, C, and D detonations depicted in Fig. 8.

explosions. However, the relative amplitudes observed inside the basin for the explosion C are close to the ones observed for the other detonations. These two observations imply a loss of energy under the explosion C. Thus, the diffracted field magnified by the vicinity of the interface appears to be defocused by this interface. The observed defocusing attenuation effect can be explained as well by the vicinity and by the convex shape of this interface.

The fields that propagate inside the basin for explosions C and D are mainly composed of well-formed Rayleigh wavetrains [see receivers f, e, d, and c, Figs 9(c) and (d)]. These wavetrains are clearly magnified in the left-hand side ascent region of the basin. This region also enhances the later arrivals, inducing a lengthening and a slight dispersion of the Rayleigh wavetrain. These effects cannot be as well observed for the explosions A and B as the wavetrains are not sufficiently well formed before arriving in this area. The amplitude of the displacement fields emitted in the left-hand side of the basin by all the explosions are comparable (see receivers a and b Fig. 9). But in the right-hand side of the basin (i.e. for the receivers k and l) the displacement field amplitude for explosion C (Fig. 9c) is 2 times the displacement for explosion A and B, and 30 per cent higher than that of explosion D. We finally notice for all explosions the lengthening of the emitted surface waves after a long travel in the basin (e.g. at receivers k and l explosion A, and at receivers a and b for explosions C and D).

3.3 Diffracted field by a multilayered basin

The aim is here to study a way of coda wave generation in a two-layer basin. The model is described in Fig. 10. Thirty-four receivers are regularly distributed at the surface with an interstation spacing of 0.33 km. Four explosions (A, B, C, and D) are
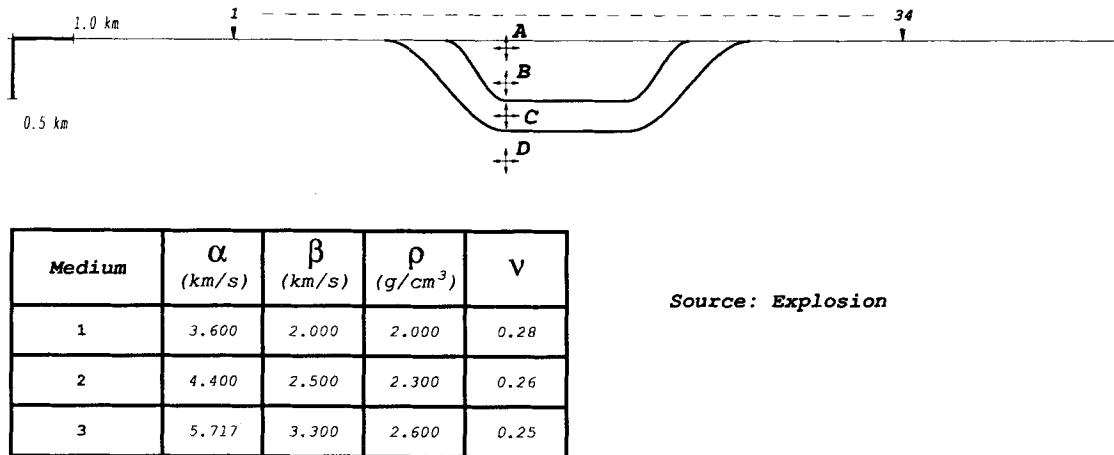
Figure 10. Multilayered medium geometry and location of the 34 receivers. The four explosions considered are denoted by A, B, C, and D in the first, second and third layers.

detonated in the left region of the three media at 50, 400, 625, and 1000 m depth respectively. The corresponding displacement fields generated are displayed in Figs 11(a), (b), (c), and (d). The displacements are given at 1 Hz and 1.8 Hz, which correspond to the S- and to the P-wave resonant frequencies, and at 3.8 Hz which is close to 2 times the P- and 4 times the S-wave resonant frequencies of medium 1. The horizontal axes show the 5 s duration time window and the vertical axes the offsets of the receivers from the source location. Non-causal signals are apparent before the first arrival [e.g. see the vertical component at 3.8 Hz Figs 11(a) and (b)]. They illustrate the aliasing effects related to an over-reduction of the spatial periodicity X_L (see Section 2).

Different diffracted fields appear with the varying depths of burial. In the case of the explosion C (Fig. 11c) the corresponding phases are well separated, therefore we use this case to describe the notations. Different phases are labelled. (i) The first observable arrival (i.e. following the non-visible direct P-wave) corresponds to the surface P-wave, P_{surf}, which propagates outside of the basin as described by Lapwood (1949), and Bouchon (1978). This phase, observed on the horizontal component at all frequencies for negative offsets and at high frequencies for positive ones, has been diffracted by the edges of the basin. Following the P_{surf}-wave (ii) a surface wave, R_1, is observed. This phase corresponds to the Rayleigh wavetrain that travelled across the basin before being emitted outside of the basin. This surface wave can be observed for both positive and negative offsets. (iii) Then two phases, R_2 and R_3, well observed at 1.8 Hz, arrive after a 1 s duration gap of ground motion. Because these phases do not continue inside and only appear at the edge of the basin, they can be interpreted as Rayleigh waves which may result from two successive interface P-waves that have backpropagated along the two interfaces from the right edge to the left side of the basin. The first one (i.e. R_2) has propagated along the second interface with the P-wave velocity of the third medium and arrives half a second before the phase R_3 which has propagated along the first interface with the P-wave velocity of the second medium.

For the explosion A buried at 50 m depth the surface P-wave and the first Rayleigh wave are the main phases appearing at all frequencies. The phase R_{2-3} corresponds to the previously described phases R_2 and R_3. The prominant phase inside the basin is a Rayleigh wave, whatever the frequency is. On the contrary in the case of explosion B buried at 400 m depth (Fig. 11b) the Rayleigh wave is replaced by a head P-wave, P_{head}, for the frequency 3.8 Hz. In this case the phases R_2 and R_3 are well separated. We also notice at 3.8 Hz that the phase R_1 observed for positive offsets results from a Rayleigh wave for explosion A while it results from a head P-wave for explosion B.

In the case of explosion C (Fig. 11c) detonated in the second medium the direct P-wave, P, is the main phase present inside the basin at 1.8 and 3.8 Hz while the Rayleigh wave stays predominant at 1 Hz. Besides the R_1 branch observed at all frequencies, a P_{surf} branch is also diffracted for positive offsets. At 3.8 Hz the phase R_3 remains the major phase observed for negative offsets. This last observation can also be made in the case of explosion D (Fig. 11d). In this last case, the fields observed are essentially made of the direct P-wave, P, and of the Rayleigh wave R_1.

4   CONCLUSIONS

We have described the discrete wavenumber–boundary integral equation method in the case of a medium made up of a half-space underlying a stack of irregularly bedded deposit layers. The method used to determine the force distribution has been detailed in the case of seismic sources located anywhere in the medium. The source site influence on the displacement field has been analysed for local distances. This study has given prominence to the defocusing effect that can be observed for certain source location versus medium geometry configurations. We also have shown the importance of the waves propagating
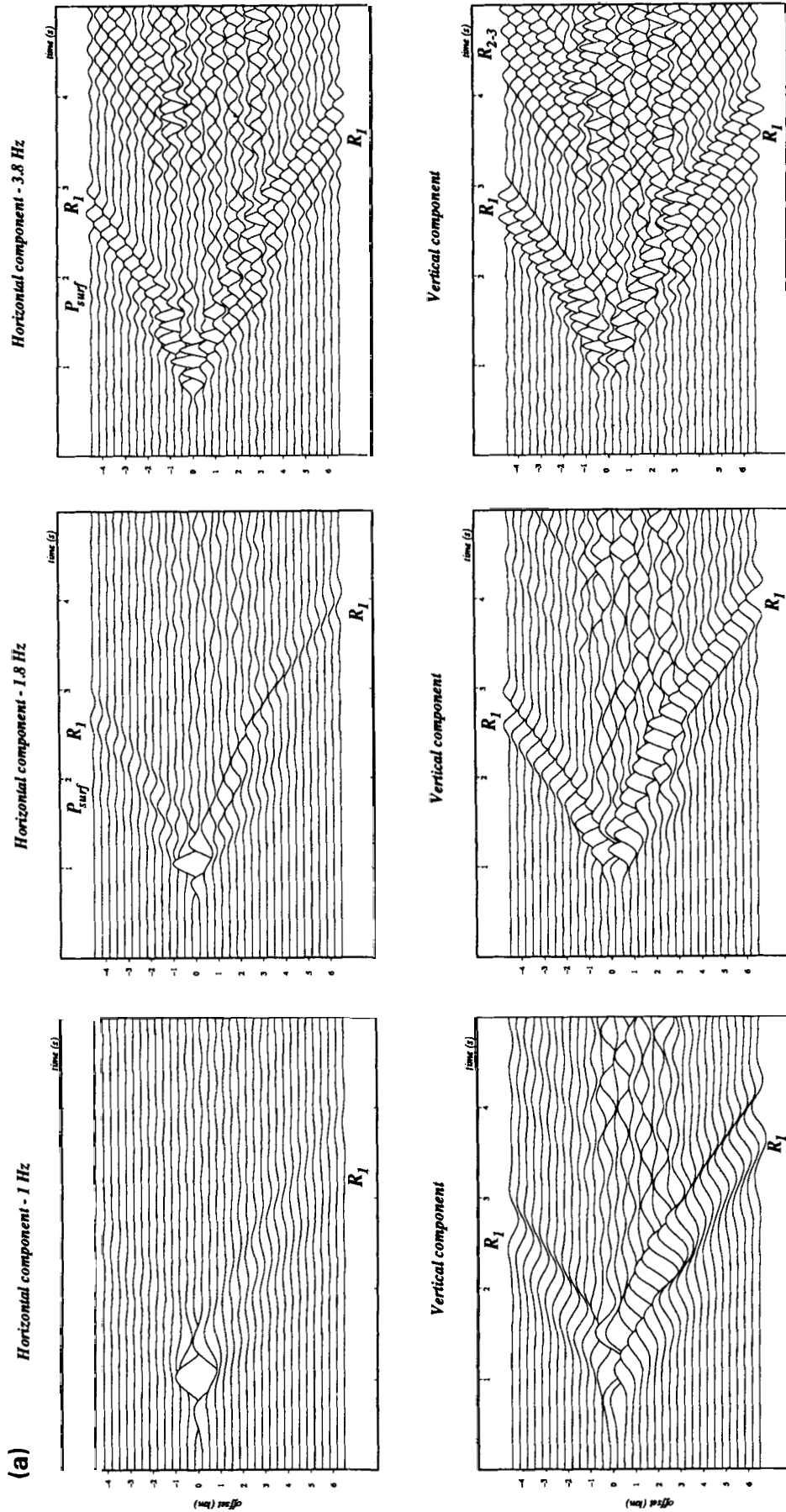
(a)

Horizontal component - 1 Hz

Vertical component

Horizontal component - 1.8 Hz

Vertical component

Horizontal component - 3.8 Hz

Vertical component

Figure 11. (a)–(d) Time versus distance horizontal and vertical displacement representations for explosions A, B, C and D, respectively. The main labelled phases are described in the text.
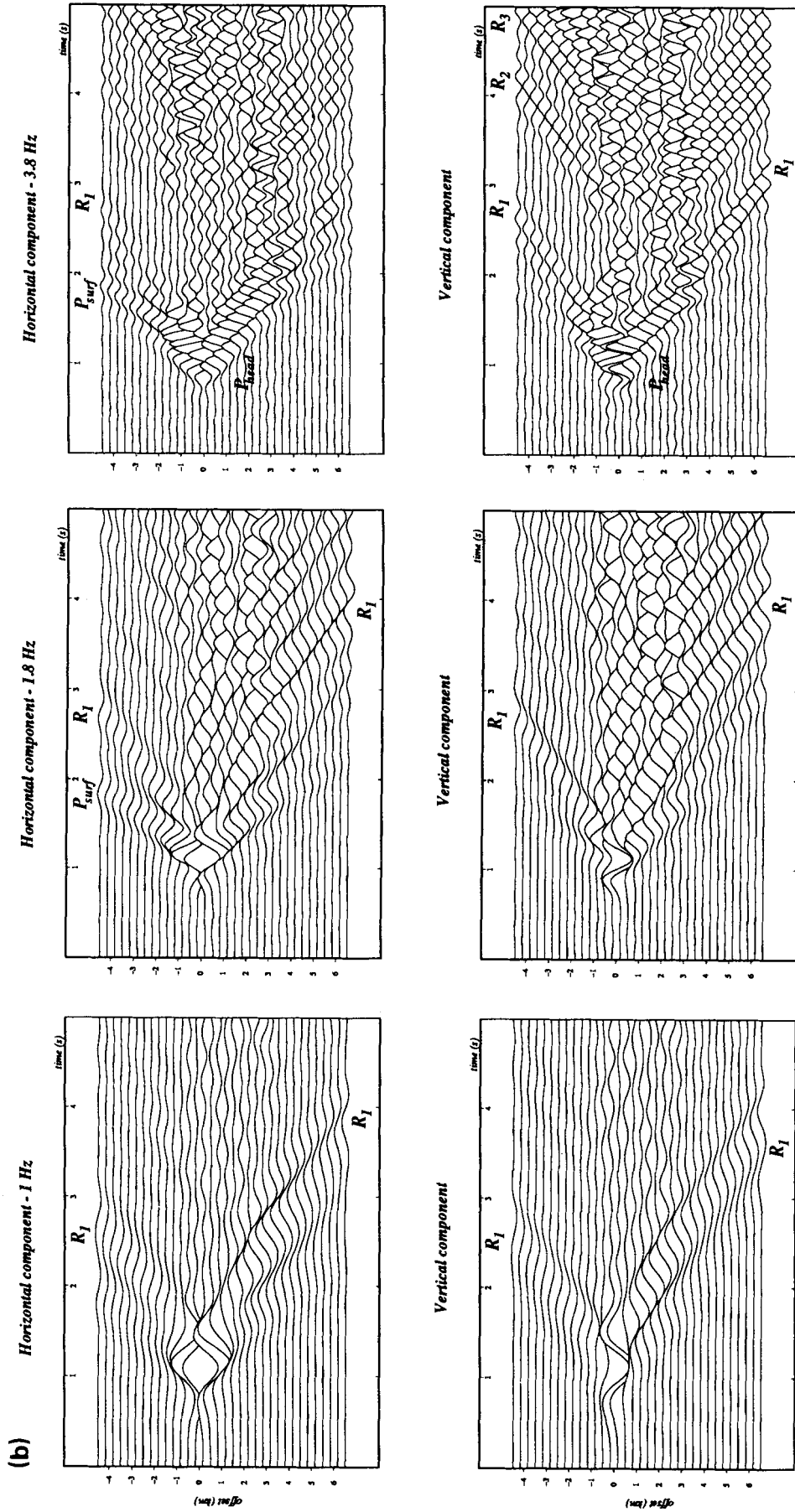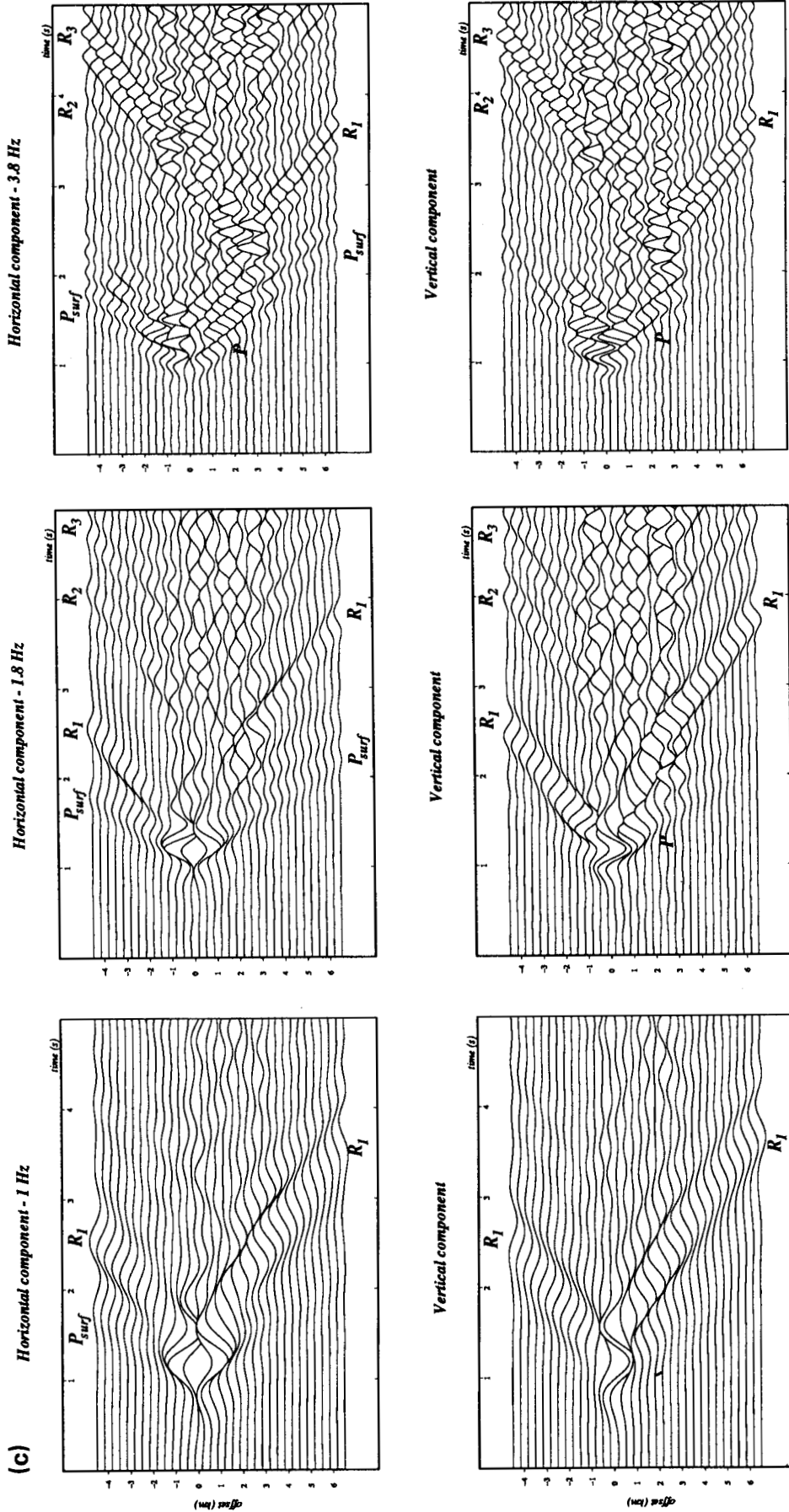
Figure 11. (continued)
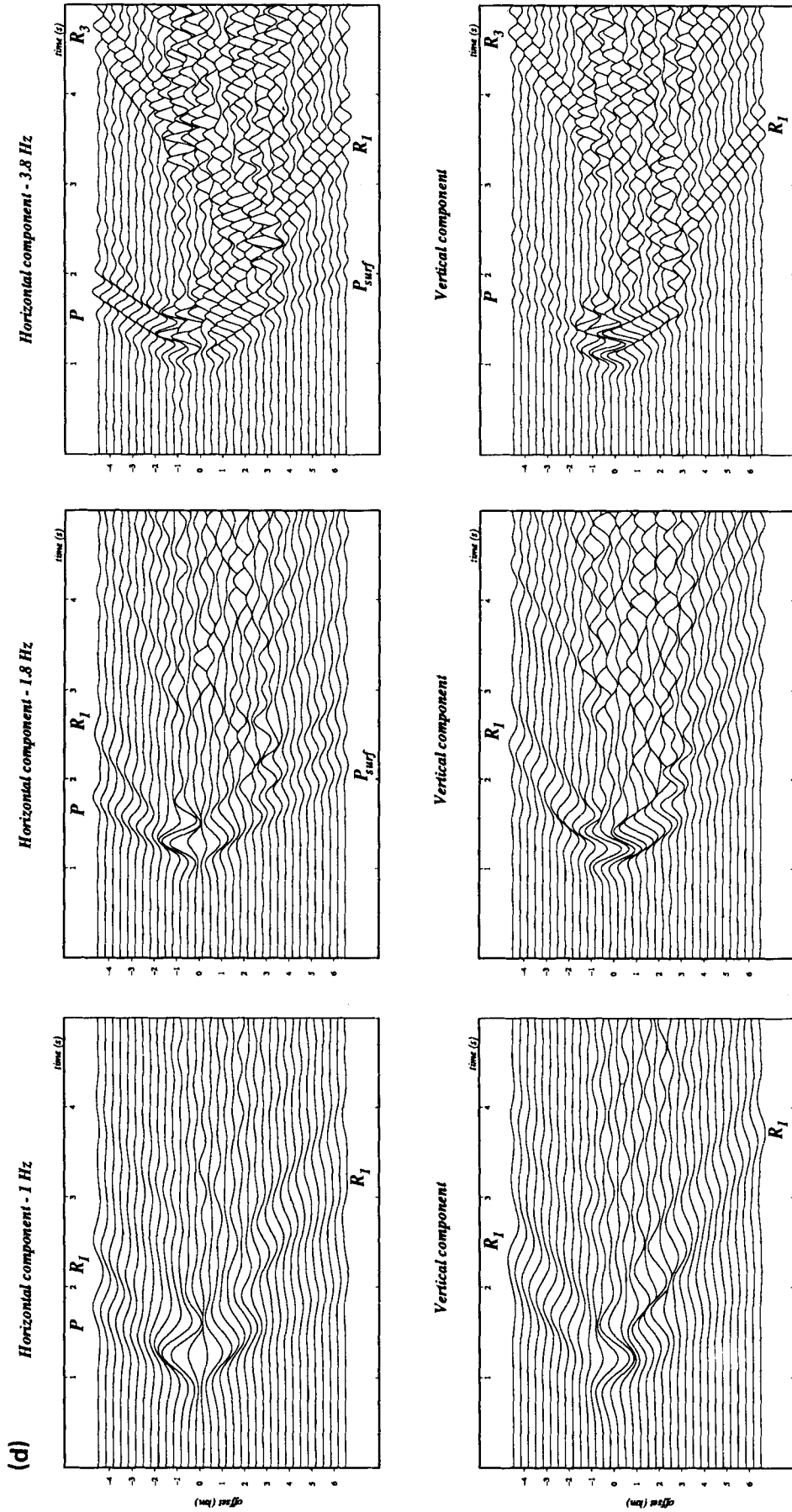
Figure 11. (*continued*)

Figure 11. *(continued)*

along the various interfaces. These waves cross the basin along its basement and reappear at its edges where they are diffracted as Rayleigh surface waves.

ACKNOWLEDGMENTS

REFERENCES

Aki, K. & Larner, K. L., 1970. Surface motion of a layered medium having an irregular interface due to incident plane SH-waves, *J. geophys. Res.*, **75**, 933–954.

Bard, P.-Y. & Bouchon, M., 1980a. The seismic response of sediment-filled valleys. Part 1. The case of incident SH-waves, *Bull. seism. Soc. Am.*, **70**, 1263–1286.

Bard, P.-Y. & Bouchon, M., 1980b. The seismic response of sediment-filled valleys. Part 2. The case of incident P- and SV-waves, *Bull. seism. Soc. Am.*, **70**, 1921–1941.

Bard, P.-Y. & Bouchon, M., 1985. The two-dimensional resonance of sediment-filled valleys, *Bull. seism. Soc. Am.*, **75**, 519–541.

Bard, P.-Y. & Gariel, J. C., 1986. The seismic response of two-dimensional sedimentary deposits with large vertical velocity gradients, *Bull. seism. Soc. Am.*, **76**, 343–366.

Bouchon, M., 1978. The importance of the surface or interface P-wave in near-earthquake studies, *Bull. seism. Soc. Am.*, **68**, 1293–1311.

Bouchon, M. & Aki, K., 1977. Discrete wavenumber representation of seismic source wave fields, *Bull. seism. Soc. Am.*, **67**, 259–277.

Bouchon, M., Campillo, M. & Gaffet, S., 1989. A boundary integral equation–discrete wavenumber representation method to study wave propagation in multilayered media having irregular interfaces, *Geophysics*, **54**, 1134–1140.

Campillo, M., 1987. L_g-wave propagation in a laterally varying crust and the distribution of apparent quality factor in central France, *J. geophys. Res.*, **92**, 12 601–12 614.

Ferguson, J. F., 1988. Body-wave magnitude variation at Yucca Flat, Nevada, *Bull. seism. Soc. Am.*, **78**, 863–872.

Gaffet, S. & Bouchon, M., 1989. Effects of two-dimensional topographies using the discrete wavenumber–boundary integral equation method in P–SV cases, *J. acoust. Soc. Am.*, **85**, 2277–2283.

Kawase, H. & Aki, K., 1989. A study on the response of a soft basin for incident S, P, and Rayleigh waves with special reference to the long duration observed in Mexico City, *Bull. seism. Soc. Am.*, **79**, 1361–1382.

Lamb, H., 1904. On the propagations of tremors at the surface of an elastic solid, *Phil. Trans. R. Soc. Lond.*, A, **203**, 1–42.

Lapwood, E. R., 1949. The disturbance due to a line-source in a semi-infinite elastic medium, *Phil. Trans. R. Soc. Lond.*, A, **242**, 63–100.

Sánchez-Sesma, F. J. & Esquivel, J. A., 1979. Ground motion on alluvial valleys under incident plane SH-waves, *Bull. seism. Soc. Am.*, **69**, 1107–1120.

Sánchez-Sesma, F. J., Chávez-García, F. J. & Bravo, M. A., 1988. Seismic response of a class of alluvial valleys for incident SH-waves, *Bull. seism. Soc. Am.*, **78**, 83–95.

Tucker, B. E. & King, J. L., 1984. Dependence of sediment-filled valley response on input amplitude and valley properties, *Bull. seism. Soc. Am.*, **74**, 153–165.